Evaluating Propulsor Mechanical Flow Power in Powered Aircraft Wind Tunnel Experiments

Nina Siu[*], Neil Titchener[†], Cécile Casses[‡], Arthur Huang[§], Alejandra Uranga[¶], Mark Drela[‖] and Edward Greitzer[**]

Massachusetts Institute of Technology, Cambridge, MA 02139, U.S.A.

This paper describes a methodology for evaluating propulsor mechanical flow power on a 1:11 scale, electrically powered, wind tunnel model of a boundary layer ingesting (BLI) aircraft. The use of a full aircraft aerodynamic configuration precluded direct in-situ measurements of the mechanical flow power, a key metric for BLI aircraft performance. The measured electrical power thus had to be converted to flow power through two sets of supporting experiments. The first set of experiments were flow power measurements with the propulsor in a small wind tunnel which replicates the incoming flow conditions of the powered wind tunnel test. The second set were motor calibration experiments that allowed the motor losses and aerodynamic inefficiencies to be determined separately, giving insight into the motor and the aerodynamic operating point of the propulsor. Using this combined approach, the measurements of electrical power were converted to mechanical flow power with an experimental uncertainty of less than 1%.

Nomenclature

A_{fan}	fan face area
C_{p_t}	stagnation pressure coefficient $= (p_t - p_{t0})/q_0$
C_{P_E}	electrical power coefficient $= P_E/(\rho U_{\text{tip}}^3 A_{\text{fan}})$
dA	elemental area
D	tunnel diameter (=6 inches)
DC_{60}	distortion coefficient within 60° section
i	electrical current
k	screen pressure drop constant $= \Delta p_t/q_0$
$\dot{m}$	mass flow
$\hat{\mathbf{n}}$	unit normal vector
p	static pressure
p_t	stagnation pressure
p_{t0}	tunnel stagnation pressure
q_0	tunnel dynamic pressure $= \frac{1}{2}\rho V_0^2$
Re_D	Reynolds Number based on five-hole probe diameter
P_E	electrical power
P_K	mechanical flow power
P_{K_0}	tunnel freestream mechanical flow power

[*]Graduate Student, Dept. of Aeronautics and Astronautics, ninasiu@mit.edu, AIAA Member.
[†]Postdoctoral Associate, Dept. of Aeronautics and Astronautics, nat25@mit.edu, AIAA Member.
[‡]Graduate Student, Dept. of Aeronautics and Astronautics.
[§]Research Engineer, Dept. of Aeronautics and Astronautics, AIAA Member.
[¶]Research Engineer, Dept. of Aeronautics and Astronautics, auranga@mit.edu, AIAA Member.
[‖]Terry J. Kohler Professor of Fluid Dynamics, Dept. of Aeronautics and Astronautics, AIAA Fellow.
[**]H.N. Slater Professor of Aeronautics and Astronautics, Dept. of Aeronautics and Astronautics, Honorary AIAA Fellow.

P_S	shaft power
Q	motor torque
u	repeatability of quantity
U_{tip}	rotor tip speed
v	voltage
$\mathbf{V}$	total velocity vector
V_0	GTL 1x1 foot wind tunnel velocity
V_{fan}	axial fan face velocity
V_x	velocity component in the streamwise direction
x, y, z	tunnel axes: x is streamwise and z is vertical
η_f	fan efficiency $= P_K/P_S$
η_m	motor efficiency $= P_S/P_E$
η_o	overall propulsor efficiency $= P_K/P_E$
σ	measurement uncertainty
ρ	air density
ϕ	flow coefficient $= V_{\text{fan}}/U_{\text{tip}}$
ψ	stagnation pressure rise coefficient
Ω	fan angular velocity, wheel speed
$\overline{(\ )}$	mass-averaged quantity

I. Introduction

A. Background

There is growing interest in using boundary-layer ingesting (BLI) propulsion systems, in which part of the vehicle's boundary layers pass through the propulsion stream. By combining the propulsive jet and the vehicle wake a BLI propulsion system reduces the mixing losses in both the wake and jet, decreasing the power needed to perform a given mission. Analytical studies have found potential benefits in the region of 5–10%.[1–3]

In 2008, NASA initiated the N+3 Program with the aims of establishing new trends in civil aircraft design, determining enabling technologies and defining areas that require investment for aircraft in the 2030–35 timeframe. During the first phase of this program, an MIT, Aurora Flight Sciences and Pratt & Whitney team developed the conceptual designs for two boundary layer ingesting aircraft that showed major potential for fuel burn reductions.[4]

In Phase II of the program, one of these designs (the D8 or Double-Bubble[5]), has been experimentally investigated, providing the first back-to-back experimental comparison between a BLI and non-BLI airframe/propulsion system for civil aircraft. This paper reports results from this study on the supporting experiments that were necessary for determining the boundary layer ingestion benefit.

B. Overview of the Experiments and Experimental Goals

To determine the aerodynamic benefit of BLI, a 1:11-scale powered model was designed, constructed and tested in the NASA Langley (LaRC) 14x22 foot Subsonic Wind Tunnel.[6] To achieve a direct comparison, two D8 models were examined: one featuring BLI, referred to as the integrated configuration, and the other featuring conventional propulsors within nacelles, referred to as the podded configuration. The two configurations are shown schematically in Figure 1. Both models are powered with two Aero-naut TF8000 ducted fans driven by Lehner 3040 electric motors.

It is not possible to separate thrust and drag for a boundary layer ingesting aircraft. As a result, our principal metric cannot be based on a force balance. Instead, our chosen metric for BLI benefit is the propulsive power needed at the simulated cruise condition of no net horizontal force on the aircraft. The power is a surrogate for fuel burn.

The power provided to the propulsors of the wind tunnel D8 model can be quantified at three levels. First is the electrical power provided to the motors, P_E, second is the shaft power, $P_S = \eta_m P_E$ (where η_m is the motor efficiency) and third is the net mechanical flow power produced by the propulsors, $P_K = \eta_f P_S$

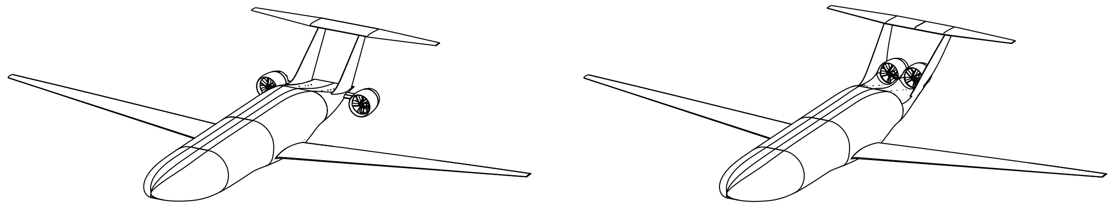

(a) podded configuration (b) integrated configuration

Figure 1. Schematic isometric drawings of the two NASA/MIT N+3 D8 configurations

(where η_f is the fan efficiency). P_K is also defined as the mass flux of stagnation pressure,

$$P_K = \oiint (p_{t\infty} - p_t)\mathbf{V} \cdot \hat{\mathbf{n}}\, \mathrm{dA}. \tag{1}$$

A preliminary assessment of the experiments, using electrical power as the initial metric was presented by Uranga et al.[7] While electrical power is the quantity measured directly in our experiments, it is not of primary interest Shaft power directly relates to specific fuel consumption and hence efficiency, which is the principal metric for an optimized gas turbine. In the present set of experiments, however, the turbomachinery is not necessarily optimal, and thus it is desirable to eliminate the effect of turbomachinery performance on the BLI benefit. To do this we have adopted the mechanical flow power as our metric of performance. Measuring this quantity eliminates the effect of the propulsion system and isolates the aerodynamic benefit of BLI.

The process of going from the measured electric power to the desired quantity of mechanical flow power is the subject of this paper. In this paper we describe the calculations and experiments required to convert the electrical measurements to aerodynamic quantities of interest. The paper also includes an account of the simulation of the incoming fuselage boundary layer and an analysis of the experimental uncertainties associated with this conversion.

II. Experimental Approach

A. Description of the Experiments

The conversion of electrical power measurements, P_E, to mechanical flow power, P_K, has been carried out through two sets of supporting experiments at the MIT Gas Turbine Laboratory (GTL): (i) overall propulsor performance mapping and (ii) electric motor efficiency calibration. The process by which the electrical power is converted to mechanical flow power is presented in the flow chart of Figure 2. In the propulsor performance mapping experiment, P_E is mapped to P_K using the overall efficiency ($\eta_o = \eta_m \eta_f$). This allows us to determine the mechanical flow power at propulsor flow coefficients and wheel speeds of interest. The second set of supporting experiments is the motor calibration assessment used to determine the motor and controller electronics efficiency. The results from the two experiments can be combined to establish the fan efficiency, η_f.

B. Propulsor Turbomachinery

The fan used in the propulsor is an Aero-naut TF8000, which has a five-bladed rotor and a four-bladed stator, both fabricated from carbon composites. The hub of the TF8000 houses the Lehner motor that drives the rotor. A frontal view of one of the propulsors is presented in Figure 3. The TF8000 has a custom-designed aluminum nacelle, which is designed to be inserted into the nacelle external housing for both the podded and integrated configurations, so that identical propulsors can be installed in both models.

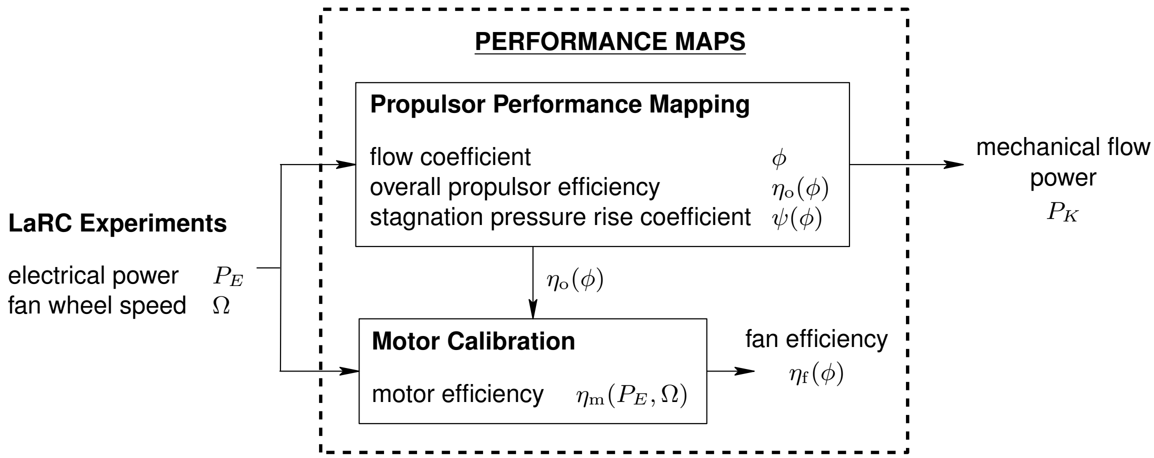

Figure 2. Path to convert LaRC measurements of P_E and Ω to P_K through the supporting MIT GTL experiments

Figure 3. Front view of the Aero-naut TF8000 electric ducted fan

C. Motor calibration

1. Setup

The conversion of electrical power, P_E, to mechanical flow power, P_K, requires the assessment of the motor efficiency, which is the ratio of shaft power, P_S, to electrical power. The motor efficiency is found through calibration of the electrical motor torque, Q, as a function of P_E (the product of electrical voltage v and current i) and shaft rotational speed, Ω.

$$\eta_m = \frac{P_S}{P_E} = \frac{Q\Omega}{iv} \tag{2}$$

The torque provided to the shaft is measured using the motor calibration rig shown in Figure 4. A compression load cell is employed to measure torque via a moment arm and perpendicular force. The motor shaft rotational speed is acquired from the back-EMF signal from the motor, and the current and voltage are obtained from the power supply.

Different-sized APC propellers (10x07, 10x08, 10x09) were attached to the motor shaft to vary the loading on the motor. The propellers bracketed the conditions experienced by the motors during the LaRC wind tunnel experiments. Each propeller was tested with each motor at least four times.

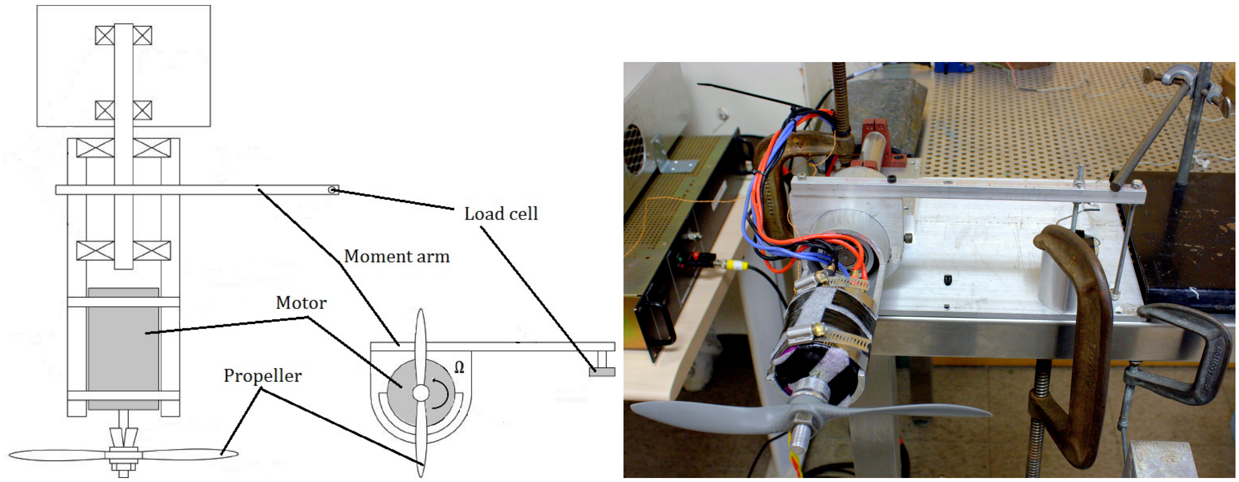

(a) (b)

Figure 4. Dynamometer rig for torque measurement

2. Motor Efficiency

Contours of motor efficiency based on electrical power, P_E, and shaft rotational speed, Ω are shown in Figure 5. This motor efficiency map was used in subsequent experiments to determine the shaft power given P_E and Ω.

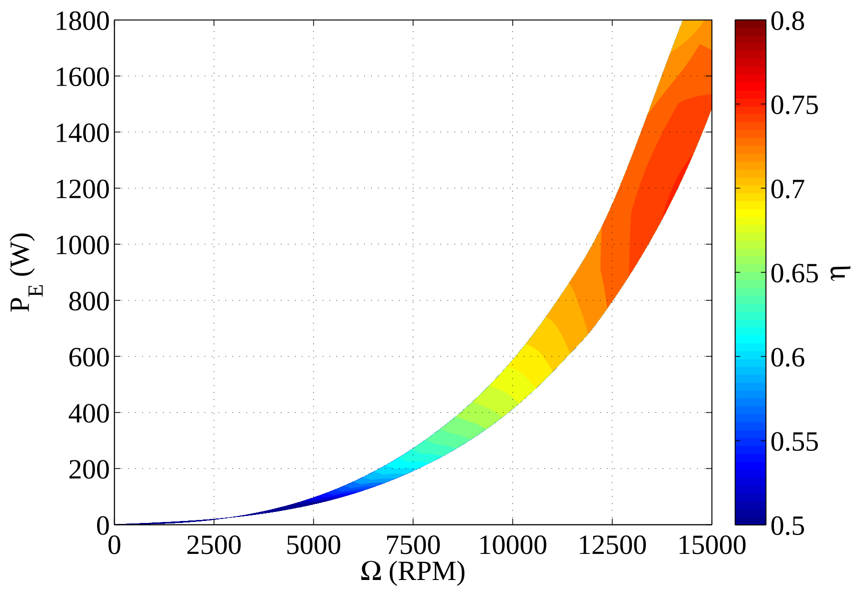

Figure 5. Contours of motor efficiency, η_m, as a function of electrical power, P_E, and wheel speed, Ω

D. Propulsor Characterization Setup

The overall propulsor performance mapping was conducted in the 1x1 foot, open-circuit, low-speed wind tunnel in the MIT Gas Turbine Laboratory. Each propulsor can be attached to the wind tunnel working section which is designed to create both non-distorted and distorted inflow conditions.

As described above in Section B, the propulsors can be removed from their housing on the airframe and inserted into the working section of the 1x1 foot wind tunnel. Figure 6 shows a schematic of the 1x1 foot working section with a propulsor. There is a contraction which reduces the wind tunnel exit flow from a 1x1 foot square to a 6 inch diameter circular cross-section, a constant-area duct which includes a slot for the insertion of distortion screens to simulate the boundary layer, and another, smaller contraction which mates the 6 inch duct to the 5.7 inch diameter propulsor.

To replicate the non-uniform flow ingested by the propulsor in the integrated case, distortion screens were installed upstream of the TF8000 rotor (see Figure 6) at an approximate $L/D = 1.5$. When the podded configuration was simulated, a blank screen was inserted into the slot. The design, testing and evaluation of different screens is presented in Section III.

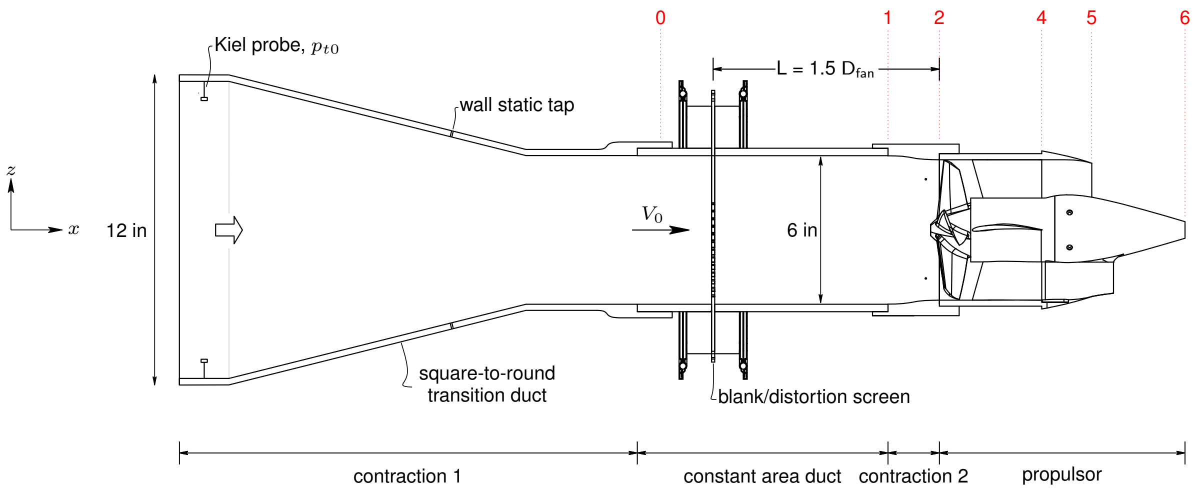

Figure 6. MIT GTL 1x1 ft wind tunnel working section setup and station designations

The flow was surveyed using a standard axial, conical-head, five-hole probe from Aeroprobe, as in Figure 7. The five-hole probe was calibrated against a range of pitch and yaw angles (every 2° between ±30°) at different Reynolds numbers (probe Re_D between 4000 and 10000) in the 1x1 foot wind tunnel to bracket the range of flow conditions for the experiments.

To measure the mechanical flow power input by the propulsor, the flow needs to be surveyed at planes upstream and downstream of the propulsor. Five-hole probe area traverses were thus performed at Station 1 and Station 5. As the TF8000 rotor is $1.5D$ downstream of the distortion screen, their potential fields do not interact significantly, and traverses at Station 1 were performed without the TF8000 propulsor installed. For the traverses downstream of the propulsor, the probe tip was located at the trailing edge of the nacelle, Station 5.

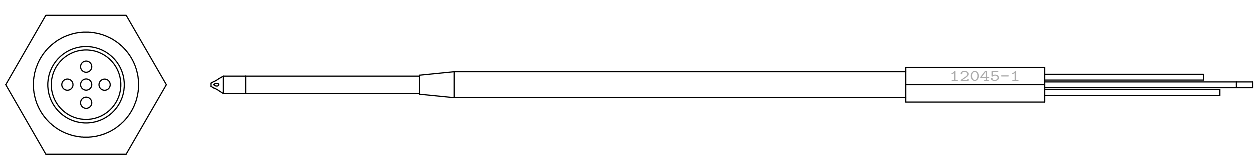

Figure 7. Front (enlarged) and side views of the Aeroprobe conical-head five-hole probe

The operating point of the TF8000 is controlled by varying the freestream tunnel velocity. This allows the mass flow, $\dot{m}$, or equivalently, flow coefficient, ϕ, to be varied at a given wheel speed.

$$\phi = \frac{V_{\text{fan}}}{U_{\text{tip}}} \tag{3}$$

In Equation 3 the fan velocity, V_{fan}, is the axial velocity across the fan face, calculated using the mass flow from the five-hole probe measurements,

$$V_{\text{fan}} = \frac{\dot{m}}{\rho A_{\text{fan}}} = \frac{1}{A_{\text{fan}}} \int V_x \, \text{dA}. \tag{4}$$

The stagnation pressure rise across the propulsor is reported non-dimensionally as a pressure rise coefficient,

$$\psi = \frac{\Delta \overline{p_t}}{\rho\, U_{\text{tip}}^2}, \tag{5}$$

where $\Delta \overline{p_t}$ is the difference in mass-averaged values of stagnation pressure from Station 1 to Station 5.

E. Determination of Operating Point

For a given fan wheel speed, the operating point of the propulsor is uniquely determined from the electrical power, such that

$$\frac{P_E}{\rho U_{\text{tip}}^3 A_{\text{fan}}} = \frac{\phi\psi(\phi)}{\eta_o(\phi)}. \tag{6}$$

The terms on the left-hand side of Equation 6 are experimental measurements, and the terms on the right-hand side are from the performance map generated from the supporting experiments. η_o and ψ are functions of flow coefficient and fan wheel speed, and for given values of P_E and wheel speed, there is a unique value of ϕ that satisfies the equality. The flow coefficients at the operating points during the LaRC wind tunnel testing, are not directly known, but the performance map generated in the 1x1 foot wind tunnel experiments can be used to determine them. Figure 8 illustrates how we determine the fan and motor efficiencies from the LaRC operating point that is defined by P_E and Ω. Given the flow coefficient, the overall efficiency, fan efficiency and pressure rise coefficients can be calculated as $\eta_o(\phi)$, $\eta_f(\phi)$ and $\psi(\phi)$.

III. Simulation of Distorted Inlet Flow to Propulsor

To create an inlet distortion similar to that ingested by the fan in the LaRC experiments, distortion screens were designed and fabricated. The screens were located 1.5 fan diameters upstream of the TF8000 fan. Three different screens were utilized. One corresponded to no distortion, as with the non-BLI, podded D8 configuration, where the installed screen just continued the constant area of the local tunnel section. The other two levels of distortion, referred to as "nominal" and "heavier" distortion, were designed to bracket the fuselage boundary layer stagnation pressure profile for the integrated D8 configuration. This desired profile was acquired from full, integrated D8 calculations, and the resulting propulsor inlet plane stagnation pressure flow field is shown in Figure 10. The distortion screens had area-blocking bars that varied in thickness to provide a desired stagnation pressure distortion as in Figure 9. The distortion screens were designed from computations using Fluent and iterated experimentally until the desired distortion level and profile was achieved.

An effective stagnation pressure drop constant, k, relates the mass-averaged stagnation pressure drop across the screen to the tunnel dynamic pressure, q_0.[8] Variations in the constant k were within the accuracy of the pressure transducer (0.5%) across the tested range of operating points.

$$k = \frac{\Delta \overline{p_t}}{q_0} \tag{7}$$

The traversed area at the fan inlet plane was discretized radially and circumferentially. The radial spacing was distributed to give equal area to each ring of cells, and there was equal circumferential distribution of measurement points. The inlet measurement grid is shown in Figure 11(a). The black lines denote the borders of the individual cells, and the red dots correspond to the measurement locations for the five-hole probe tip. The blue line denotes the radius of the local tunnel section. The measured stagnation pressure field without flow distortion is plotted in Figure 11(b).

Figures 11(c) and 11(d) show the inlet flow field for the nominal and heavier distortion cases. The distortion produced is vertically stratified with the heavier distortion flow contours showing a larger region of reduced stagnation pressure compared to the nominal distortion. This difference can also be seen in Figure 12 which gives the profiles of non-dimensional stagnation pressure, non-dimensionalized by freestream dynamic pressure, along the vertical centerlines for the experiments, and the centerline C_{p_t} profile at the fan inlet plane from CFD results for the integrated D8 airframe.[9]

The consistency of the growing boundary layer along the inner walls of the wind tunnel across all three of the cases in Figure 11 and the horizontal symmetry within the two distorted cases imply no unexpected

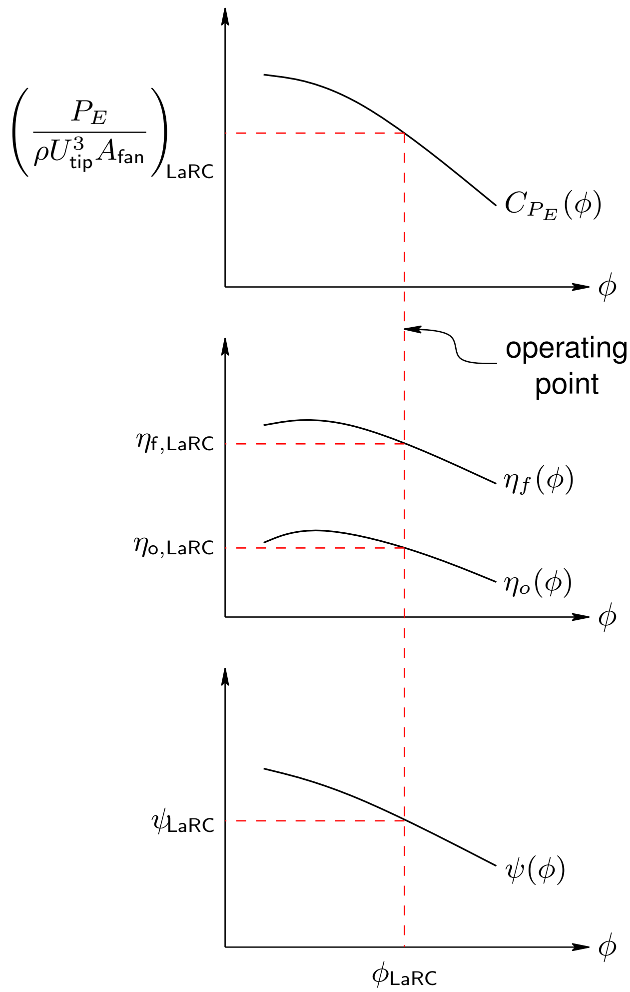

Figure 8. Mapping of fan performance characteristics measured in the supporting experiments to the LaRC experimental data using the flow coefficient, ϕ, which is uniquely defined by the LaRC measurements and the measured electrical power curve, $C_{P_E}(\phi)$

flow structures within the tunnel working section itself and negligible leaks in the junctions between wind tunnel sections.

The overall level of distortion for each screen can also be characterized using standard distortion metrics; here we use the DC_{60} distortion,

$$\text{DC}_{60} = \frac{p_{t0} - (p_{t1})_{60}}{1/2 \rho V_0^2}, \tag{8}$$

where $(p_{t1})_{60}$ is the mass-averaged stagnation pressure within the $60°$ sector of greatest distortion, as sketched in Figure 11(b). Values for DC_{60} and screen pressure drop constant k are provided in Table 1 below long with the results for a complete aircraft calculation. The screen constant for the non-distorted case is nonzero, because the measurements included losses in the tunnel wall boundary layer.

IV. Propulsor in Uniform Inlet-Flow

The mechanical flow power ingested by the propulsor, $P_{K\text{in}}$, was determined using the screen pressure drop constants in Table 1 and the tunnel velocity,

$$P_{K\text{in}} = P_{K_0} - k\frac{1}{2}\rho V_0^3 A_0. \tag{9}$$

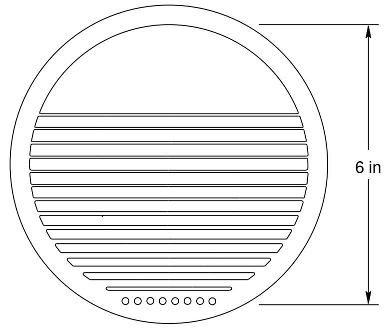

Figure 9. Nominal distortion screen design

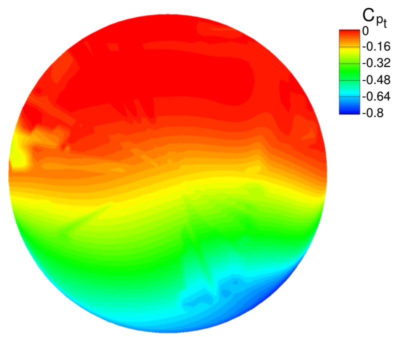

Figure 10. Contours of C_{p_t} from full aircraft simulations at cruise

The mechanical flow power out of the propulsor, $P_{K\text{out}}$, was found from five-hole probe traverses at the propulsor nozzle exit. Unlike the inlet-flow characterization, the performance of the TF8000 does not scale with the tunnel conditions, and thus cannot be represented by a constant. Nozzle-plane flow surveys were performed for multiple operating points as appropriate.

As with the inlet five-hole probe surveys, the traversed area at the propulsor exit plane was discretized radially and circumferentially; however, the exit grid was tailored to align with the trailing edge profiles of the stator blades. Higher-density grid points were used near the stators to better resolve their wakes. A bifurcation through which the motor power lines run is located immediately downstream of the bottom stator, blocking access for the five-hole probe, so the exit flow survey does not capture a full 360° area, as in Figure 13(a). The black lines denote the borders of the individual cells, and the red dots correspond to the measurement location for the probe tip of the five-hole probe. The blue line denotes the radius of the nacelle trailing edge, and the trailing edge profile of the stators are denoted in green. A midpoint integration method was used to evaluate the integral for P_K,

$$P_K = \sum_i (p_{t0} - p_t)_i \, (\mathbf{V} \cdot \hat{n})_i \, \mathrm{dA}_i. \tag{10}$$

The five-hole probe traverses at the nozzle plane provide the exit mechanical flow power of the propulsor

Table 1. Distortion screen constants

Distortion Level	DC_{60}	k
None	0.057	0.057
Nominal	0.664	0.278
Heavier	0.894	0.389
CFD	0.721	0.262

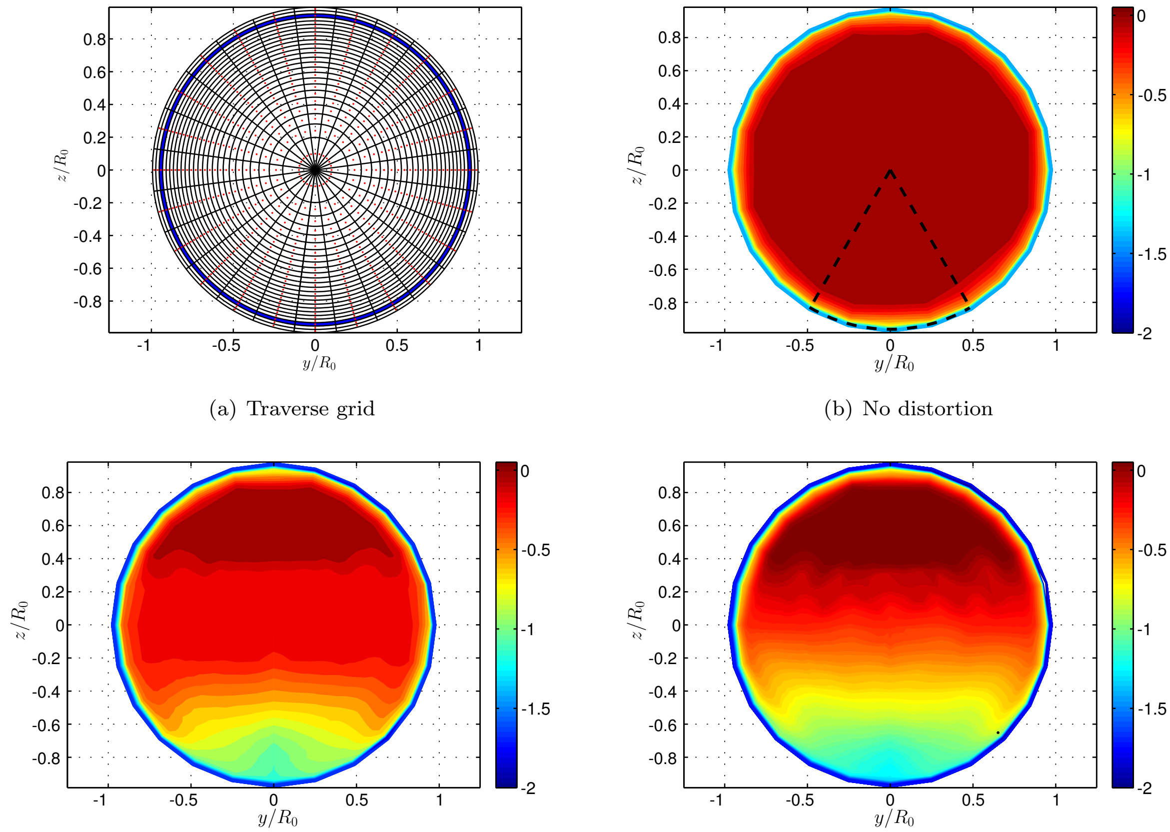

(a) Traverse grid

(b) No distortion

(c) Nominal distortion

(d) Heavier distortion

Figure 11. Inlet five-hole probe traverses. (a) Traverse measurement grid: red dots denote measurement locations, centered in cells outlined in black. Tunnel section diameter is denoted in blue. (b)-(c) contours of non-dimensional stagnation pressure C_{p_t} for varying levels of distortion at $V_0 = 27$ ms^{-1}.

as in Figure 13(b), which shows contours of non-dimensional stagnation pressure for non-distorted operation at a flow coefficient of $\phi = 0.39$. The wakes of the three traversed stators and higher loss regions near the hub on the suction side of each stator can be seen.

Figures 14-15 show the performance characteristics for the propulsor with no distortion. Measurements of overall efficiency are from the five-hole probe surveys at the inlet and nozzle planes and the monitored electrical power input to the system. The dependence on wheel speed is because the motors operate more efficiently at higher speeds. The motor efficiency (P_S/P_E), determined using the motor calibration map generated from the torque measurements for the tested operating points, is shown in Figure 15. The motor efficiency is weakly dependent on the operating condition and strongly dependent on the wheel speed.

The ratio of mechanical flow power to shaft power is the fan efficiency, $\eta_f = P_K/P_S$, which can also be represented as the ratio of overall propulsor and electric motor efficiencies, $\eta_f = \eta_o/\eta_m$. Fan efficiencies at multiple wheel speeds are given as functions of flow coefficient ϕ in the Figure 16. Compared with the overall efficiency, the η_f characteristics are much closer to a single characteristic; fan efficiency captures the aerodynamic losses for the flow through the rotor and stator, and the internal nacelle flow passages.

V. Effect of Inlet Distortion on Propulsor Performance

To fully characterize the propulsor performance, we also measured the performance of the TF8000 in distortions representative of the integrated D8 fuselage flow. The exit stagnation pressure fields with inlet distortion are shown in Figure 17(a). As in the non-distorted case, the stator wakes are visible; however there is a redistribution of the mass flow through the four stator passages.

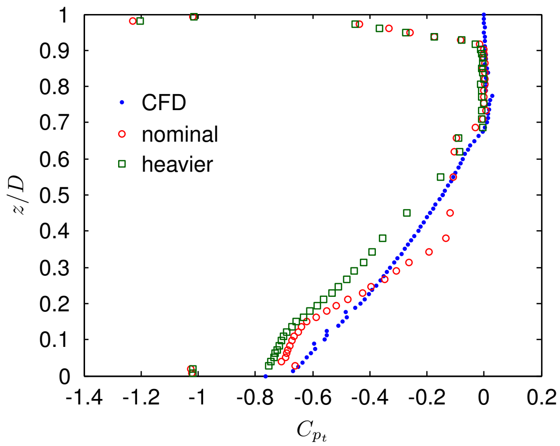

Figure 12. Centerline C_{p_t} profiles for nominal and heavier distortion levels, and for simulated cruise from full-airframe calculations

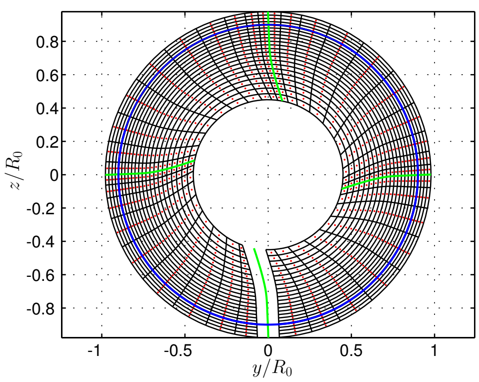

(a) Traverse grid

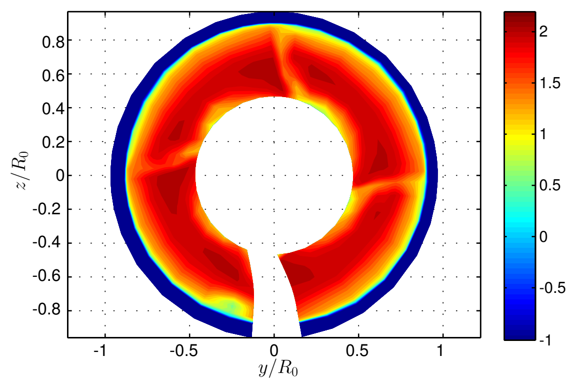

(b) C_{p_t} contours

Figure 13. Five-hole probe surveys for propulsor inlet flow field: (a) Traverse grid where each red dot denotes the measurement location, centered in each cell outlined in black. Nozzle radius is denoted in blue, and stator trailing edge profiles are in green. (b) Non-dimensional stagnation pressure, C_{p_t} contours for exit flow survey with propulsor operating at $\phi = 0.39$.

A. Overall Efficiency

Figure 18 gives the overall efficiency characteristics of the TF8000 for all distortion levels and multiple wheel speeds. The difference in overall efficiency between the non-distorted and distorted inlet flow cases is roughly 1-2%. Between the nominal and heavier distortion cases, the difference in η_o is less than 1%. The two distortion cases bracket the distortion levels seen on the D8 airframe, and we can thus infer that the propulsor sensitivity to stagnation pressure inlet distortion is small within the operating range of the experiments.

B. Fan Efficiency

Figures 19 and 20 show the electric motor and fan efficiencies. As with the overall efficiency, there is a 1-2% reduction in fan efficiency with inlet stagnation pressure distortion. The small difference between characteristics for the nominal and heavier distortion cases of the overall efficiency directly translate into the differences between distortion levels for the fan efficiency, implying that the TF8000 fan is not operating near a fall-off in performance. The low sensitivity to the level of inlet distortion also implies an appropriate representation of the inlet distortion of the D8 fuselage.

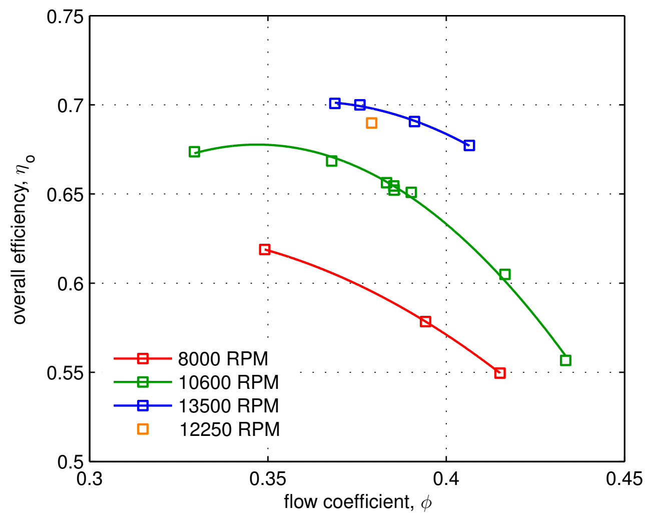

Figure 14. Overall propulsor efficiencies vs flow coefficient at multiple wheel speeds without distortion

VI. Uncertainty Analysis

A. Measurement Uncertainty

The measurement uncertainties for the 1x1 foot wind tunnel experiments depend on the accuracies of the pressure and electrical instrumentation. Assuming the measurements are statistically independent, uncertainties in the final performance metrics (the flow power P_K and the overall efficiency η_o) can be found by propagating the instrumentation accuracies through the calculation of P_K and η_o.

The uncertainty in mechanical flow power, σ_{P_K} is equal to the square root of the sum of each of the individual measurement uncertainties (i.e. each individual pressure channel measurement) multiplied by the partial derivative of P_K with respect to that quantity. Since P_K is a function of tunnel freestream and local stagnation pressures and the local axial velocity, the uncertainty of P_K is given by

$$\sigma_{P_K}^2 = \left(\frac{\partial P_K}{\partial p_{t0}}\sigma_{p_{t0}}\right)^2 + \left(\frac{\partial P_K}{\partial p_t}\sigma_{p_t}\right)^2 + \left(\frac{\partial P_K}{\partial V_x}\sigma_{V_x}\right)^2. \tag{11}$$

The uncertainties for p_{t0} and p_t above are directly from the pressure transducer, and the uncertainty for axial velocity, σ_{V_x}, is determined by propagating the uncertainties for the five pressure measurements from the five-hole probe. The partial derivatives are determined both analytically (such as expressions for the calculation of velocities) and numerically from experimental data (such as interpolation from the five-hole calibration).

Uncertainties for the propulsor overall efficiency, σ_{η_o}, are derived from uncertainties in P_K, as above, and the uncertainties of the electrical power measurements. Using the definition $\eta_o = P_K/P_E$,

$$\sigma_{\eta_o}^2 = \left(\frac{1}{P_E}\sigma_{P_K}\right)^2 + \left(\frac{P_K}{P_E^2}\sigma_{P_E}\right)^2. \tag{12}$$

The uncertainty for electrical power measurements[7] across all power levels is

$$\sigma_{P_E} = 0.011 P_E. \tag{13}$$

The overall propulsor efficiency is the final performance metric that directly converts electrical power measurements to values of mechanical flow power. For these experiments, the uncertainty on the overall efficiency is $\sigma_{\eta_o} = 0.7\%$.

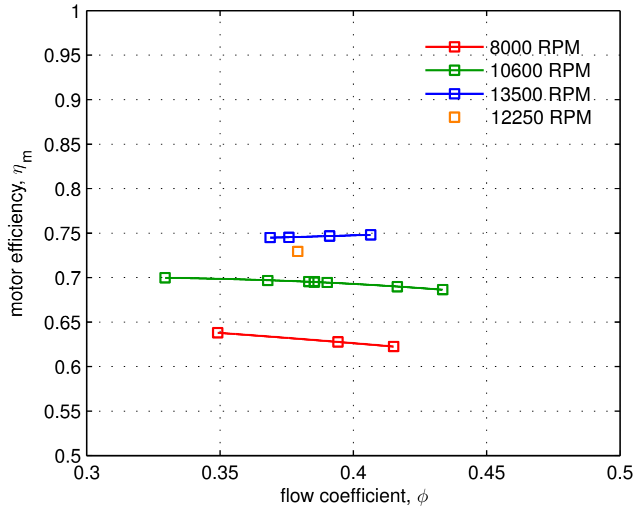

Figure 15. Electric motor efficiencies vs flow coefficient at multiple wheel speeds without distortion

B. Repeatability

The repeatability of the measurements describes the distribution of multiple measurements at repeated operating conditions. To assess repeatability, multiple traverses were performed around the operating point of the NASA Langley experiments that was closest to simulated cruise conditions. The standard deviation between the measured overall efficiencies of these repeated points and the polynomial curve fit through all of the tested operating conditions give a quantitative estimate of the experimental repeatability, which is reported here using a 95% confidence interval of this standard deviation, $u = 1.96\sigma$. Figure 21 is an expanded ("zoomed in") view of the overall efficiency as a function of flow coefficient, denoting the measurement uncertainties and repeatability relative to the curve fit.

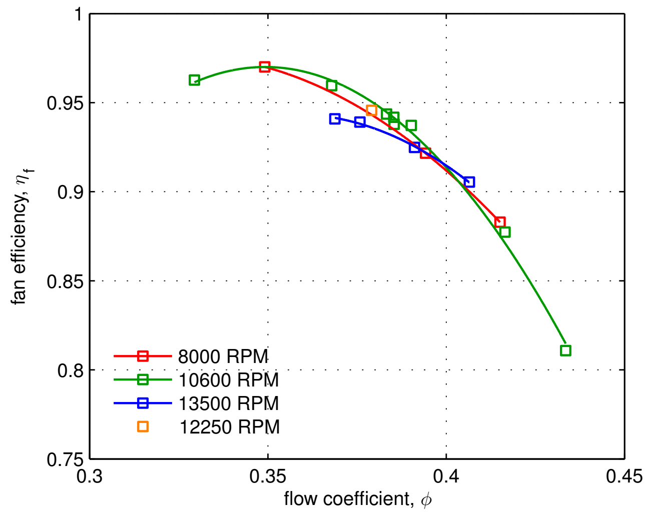

Figure 16. Fan efficiencies vs flow coefficient at multiple wheel speeds without distortion

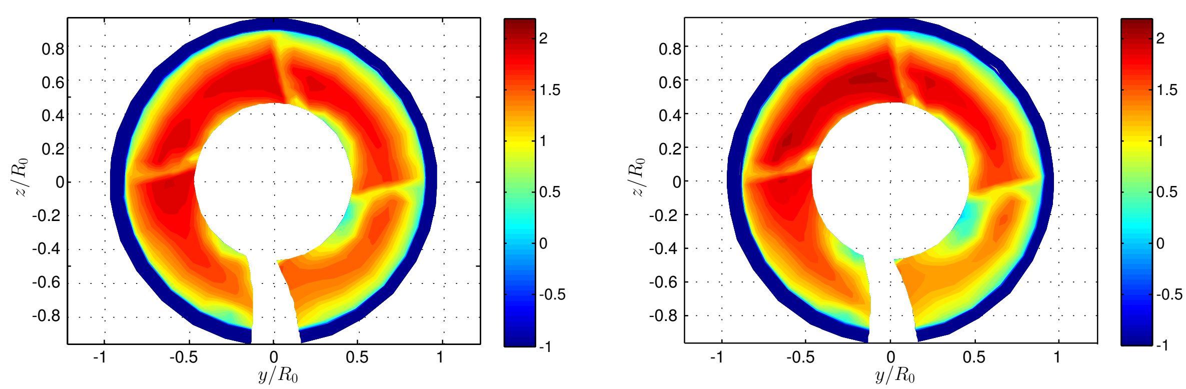

(a) Nominal distortion

(b) Heavier distortion

Figure 17. Contours of non-dimensional stagnation pressure, C_{p_t}, at the nozzle plane with the propulsor operating at $\phi = 0.39$ under nominal and heavier levels of inlet distortion

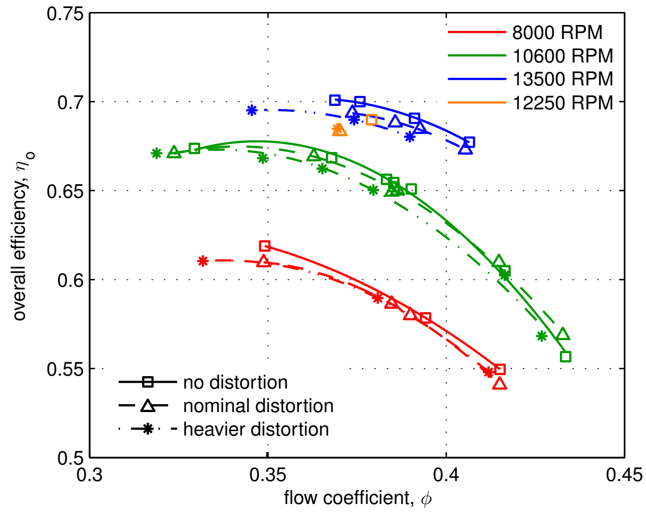

Figure 18. Overall efficiency vs flow coefficient at multiple wheel speeds for propulsor in both uniform and distorted inlet-flows

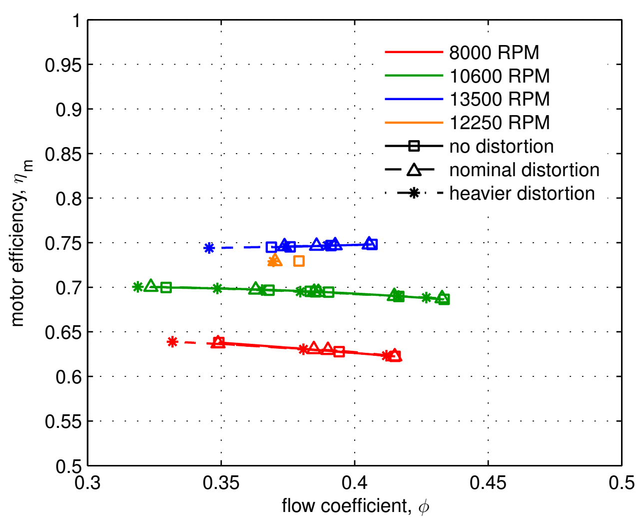

Figure 19. Electric motor efficiency vs flow coefficient at multiple wheel speeds for propulsor in both non-distorted and distorted inlet-flows

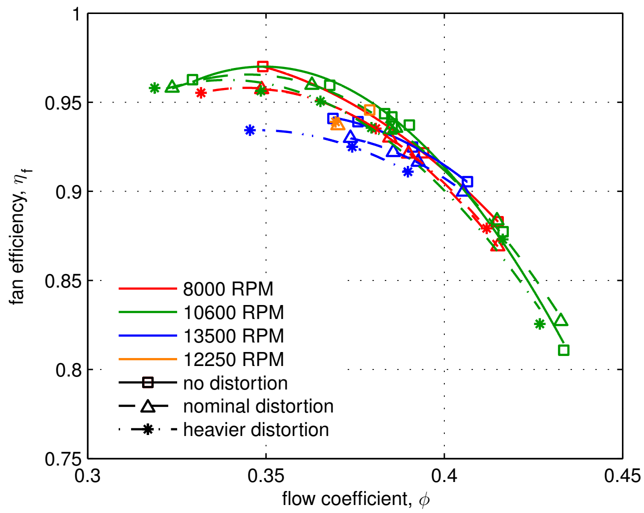

Figure 20. Fan efficiency vs flow coefficient at multiple wheel speeds for propulsor in both non-distorted and distorted inlet-flows

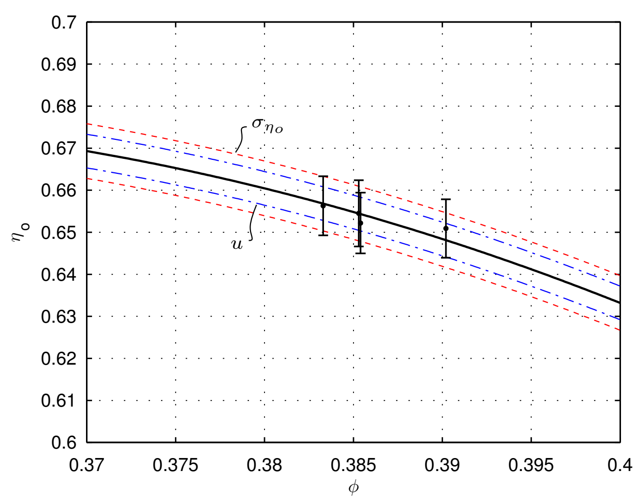

Figure 21. Zoomed-in view of overall efficiency vs. flow coefficient near the LaRC operating point. The black error bars denote the measurement uncertainty of each individual traverse. The red dashed and blue dash-dotted lines denote the measurement uncertainty, $\sigma_{\eta_o} = 0.007$, and the repeatability, $u_{\eta_o} = 0.004$, about the curve fit (black line).

VII. Conclusions and Summary

A process is described for converting electrical power measurements, in propulsion systems for powered aircraft models, to information about the net mechanical propulsor flow power. The application discussed is experiments on 1:11 scale powered aircraft wind tunnel models in the NASA Langley 14 x 22 Foot Subsonic Wind Tunnel, in which the complex geometry, and the small scale of the propulsor, makes it difficult to carry out direct flow power measurements.

The tests were aimed at the assessment of boundary layer ingestion (BLI) for an advanced civil transport aircraft. As such, they included back-to-back experiments with podded configurations in which the propulsors operated with nominally uniform flow and configurations in which the propulsors ingested the fuselage boundary layer and thus operated with combined circumferential and radial distortion.

To convert the electrical measurements to flow power information, two sets of supporting experiments were carried out subsequent to the Langley experiments. One addressed the propulsor aerodynamic behavior and was carried out in a small (1x1 foot) wind tunnel in which the inlet conditions for the propulsor could be well replicated and both the inlet and exit flow field could be measured in detail using five-hole probes. The conditions of interest included different fan speeds, different flow coefficients, and different levels of inlet distortion.

The second set consisted of measurements of the motor efficiency at different speeds and operating conditions, in order to isolate the losses associated with the motor from those generated in the propulsor. It was found that the TF8000 propulsor utilized exhibited a fan efficiency degradation of 1-2% due to boundary-layer ingestion representative of the distortion due to the fuselage boundary layer.

Using the combined approach described, the measurements of electrical power were converted to mechanical power with an uncertainty of better than 1%. Measurements of the motor efficiency were also conducted to isolate the losses associated with the motor and fan. As a result of the success of this propulsor performance mapping procedure, the methodology is planned to be again used in future powered aircraft wind tunnel tests at the NASA Langley 14x22 foot Subsonic Wind Tunnel.

Acknowledgments

This work is supported by NASA's Fundamental Aeronautics program, Fixed Wing project, through Cooperative Agreement Number NNX11AB35A. The authors would like to thank Jimmy Letendre for his management and upkeep of the wind tunnel facilities. We would also like to extend thanks to Michael Basara, Alex Feldstein, Chris Maynor and Jason Pier for their help with constructing the experimental setups.

References

[1]Plas, A. P., Sargeant, M. A., Madani, V., Crichton, D., Greitzer, E. M., Hynes, T. P., and Hall, C. A., "Performance of a Boundary Layer Ingesting (BLI) Propulsion System," No. AIAA 2007-450 in 45th AIAA Aerospace Sciences Meeting and Exhibit, 2007.

[2]Kuchemann, D. and Weber, J., *Aerodynamics of Propulsion*, McGraw-Hill, New York, 1953.

[3]Smith, L., "Wake Ingestion Propulsion Benefit," *Journal of Propulsion and Power*, Vol. 9, No. 1, 1993, pp. 74–82.

[4]et al., E. M. G., "N+3 Aircraft Concept Designs and Trade Studies, Final Report, Volume I," CR 2010-216794, NASA, 2010.

[5]Drela, M., "Development of the D8 Transport Configuration," *29^{th} AIAA Applied Aerodynamics Conference, Honolulu, HI, 27-30 June 2011, AIAA 2011-3970*, 2011.

[6]Gentry, Jr., G. L., Quinto, P. F., Gatlin, G. M., and Applin, Z. T., "The Langley 14- by 22-Foot Subsonic Tunnel: Description, Flow Characteristics, and Guide for Users," Technical Paper 3008, NASA, 1990.

[7]Uranga, A., Drela, M., Greitzer, E., Titchener, N. A., Lieu, M. K., Siu, N. M., Huang, A. C., Gatlin, G. M., and Hannon, J. A., "Preliminary Experimental Assessment of the Boundary Layer Ingestion Benefit for the D8 Aircraft," *52nd Aerospace Sciences Meeting*, National Harbor, MY, 2014.

[8]Greitzer, E., Tan, C., and Graf, M., *Internal Flows: Concepts and Applications*, Cambridge University Press, 2004.

[9]Pandya, S., Huang, A., Espitia, A., and Uranga, A., "Computatational Assessment of the Boundary Layer Ingesting Nacelle Design of the D8 Aircraft." *52nd AIAA Aerospace Sciences Meeting*, No. AIAA 2014-0907, National Harbor, MD, 2014.